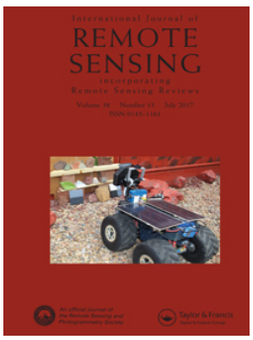

International Journal of Remote Sensing

ISSN: 0143-1161 (Print) 1366-5901 (Online) Journal homepage: http://www.tandfonline.com/loi/tres20

Laboratory spectral calibration of TanSat and the influence of multiplex merging of pixels

Hang Zhang, Yuquan Zheng, Chao Lin, Wenquan Wang, Qian Wang & Shuai Li

To cite this article: Hang Zhang, Yuquan Zheng, Chao Lin, Wenquan Wang, Qian Wang & Shuai Li (2017) Laboratory spectral calibration of TanSat and the influence of multiplex merging of pixels, International Journal of Remote Sensing, 38:13, 3800-3816, DOI: 10.1080/01431161.2017.1306142

To link to this article: https://doi.org/10.1080/01431161.2017.1306142

Published online: 07 Apr 2017.

INTERNATIONAL JOURNAL OF REMOTE SENSING, 2017
VOL. 38, NO. 13, 3800–3816
http://dx.doi.org/10.1080/01431161.2017.1306142

Taylor & Francis
Taylor & Francis Group

Laboratory spectral calibration of TanSat and the influence of multiplex merging of pixels

Hang Zhang[a,b], Yuquan Zheng[b], Chao Lin[b], Wenquan Wang[a], Qian Wang[c] and Shuai Li[b]

[a]College of Physics, Jilin University, Changchun, China; [b]Fine Mechanics and Physics, Chinese Academy of Sciences, Changchun Institute of Optics, Changchun, China; [c]National Satellite Meteorological Centre, China Meteorological Administration, Beijing, China

ABSTRACT

This article first reviews the main characteristics of the High-Resolution Hyperspectral Sensor for carbon observation Grating Spectrometer (HRHS-GS) and discusses the impact of spectral resolution on gas absorption lines. The major content of this article is the laboratory calibration of HRHS-GS, the signal-to-noise ratio (SNR), instrument line shape (ILS), and the spectral resolution of each channel were achieved. The SNR results met the mission requirements for the 0.76 μm band, but missed the requirement for the two Carbon dioxide (CO_2) bands. To address this problem, the model 'Multiplex Merging of Spectral Pixels' was established to improve the SNR by increasing the incident energy of a single spectral channel. This process would lead to spectral broadening; the spectral resolution before and after that process was obtained. The transmittance spectra before and after multiplex merging were compared by the line-by-line radiative transfer model (LBLRTM) to analyse the impact of spectral broadening on gas absorption lines. Next, the results were verified by experiment with a gas absorption cell. The results showed that 'Multiplex Merging of Spectral Pixels' could effectively improve the SNR. For the 0.76 μm band, the transmittance spectra before and after multiplex merging were almost the same; for the 1.61 μm band, the peak value of the transmittance spectra decays by about 5%; and for the 2.06 μm band, the attenuation of the transmittance spectra is smaller than 3%. Meanwhile, the spectral resolution after spectral broadening still satisfied the study's requirement.

ARTICLE HISTORY
Received 30 September 2016
Accepted 3 March 2017

1. Introduction

In view of the significant influence of CO_2, countries around the world have developed a variety of methods to monitor this gas using remote-sensing observations from space and have launched numerous optical remote-sensing monitoring instruments (Basilio, Pollock, and Hunyadi-Lay 2014; Crisp, Miller, and De Cola 2008; Kuze et al. 2006; Laurenza et al. 2014). Carbon Observing Satellite (TanSat) is the first Chinese experimental scientific satellite for monitoring the column densities of CO_2 in the atmosphere

CONTACT Wenquan Wang wangwq_jlu@sina.com Jilin University, College of Physics, Changchun, China, 130012

and identifying sources and sinks on regions scales. TanSat is under way for whole-spacecraft environment testing and will be launched in December 2016 (Liu et al. 2012; Cai, Liu, and Yang 2014; Bi et al. 2015).

TanSat has two instruments, the High-Resolution Hyperspectral Sensor for carbon observation Grating Spectrometer (HRHS-GS) and the Cloud and Aerosol Polarimetric Imager (CAPI) (Zhang, Shao, and Yan 2015; Zhang et al. 2015b). This article describes the laboratory calibration testing of HRHS-GS, mainly measuring instrument line shape (ILS), spectral resolution, and the signal-to-noise ratio (SNR) under typical illumination (5% albedo). To improve SNR without reducing spectral sampling, the model 'Multiplex Merging of Spectral Pixels' was established. The influence on transmittance spectra from spectral broadening was evaluated quantitatively through theoretical simulation and experimental results.

2. Instrument overview

HRHS-GS, the main payload of TanSat, adopts the optical system of the three-channel grating spectrometer. It consists of a telescope, a collimating system, a large-area plane diffraction grating, and a spectral imaging system. Figure 1 illustrates the optical layout of HRHS-GS. Three spectral bands share one common fore-optics. To eliminate chromatic aberration and suppress stray/scattered light, an afocal all-reflective optical system with an intermediate focus is designed as the fore-optics (Eldering et al. 2012; Cu-Nguyen et al. 2016; Bai et al. 2016). The three spectral bands are separated by the spectral relay system and isolated by dichroic beam splitters. The three beams of light pass through, respectively, a narrow bandpass filter to generate narrow-band parallel light with the wavelength range of the three spectral bands. The parallel light is focused onto the entrance slit. One large-area plane diffraction grating is used as the dispersive element to achieve high spectral resolution. The light via the entrance slit falls on the grating, the first-order diffraction light of the diffraction grating passes through the other two pieces

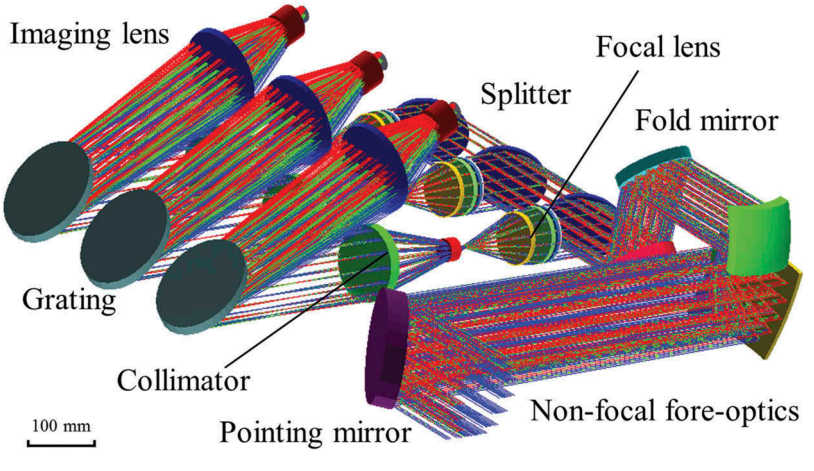

Figure 1. Optical layout of HRHS-GS.

Table 1. Summary of HRHS-GS performance requirements.

Parameter	Band 1 (O_2 A-Band)	Band 2 (weak CO_2 Band)	Band 3 (strong CO_2 Band)
Spectral range (nm)	758–778	1594–1624	2041–2081
Spectral resolution $\Delta\lambda$ (nm)	0.033–0.047	0.12–0.15	0.16–0.2
SNR	≥360:1 @5.8 × 10^{19} photons sec^{-1} m^{-2} sr^{-1} μm^{-1})	≥240:1 @2.1 × 10^{19} photons sec^{-1} m^{-2} sr^{-1} μm^{-1})	≥180:1 @1.1 × 10^{19} photons sec^{-1} m^{-2} sr^{-1} μm^{-1})
Integration time	0.293 s		
Observation modes	Nadir; Target; Sun-glint; Occultation		
Ground sample distance (@700 km)	1 km×2 km		
Swath (km)	≥20		

of quartz lens and images on a two-dimensional focal plane array (FPA), thereby obtaining fine absorption information on the atmosphere (Crisp 2015).

The detector E2V55-30 manufactured by E2 V Technologies (UK) is chosen for the 0.76 μm band, the detector is 1252 × 576 pixel arrays with 22.5 μm × 22.5 μm pixels. 320 pixels are used out of the 576 in the spatial dimension parallel to the entrance slit; in order to improve SNR, 16 adjacent pixels are merged to produce up to 20 spatially averaged 'super pixels'.

For the 1.61 μm and 2.06 μm bands, the detector uses mercury cadmium telluride (HgCdTe) as the photosensitive material. It consists of a 500 × 240 pixels array, with a pixel pitch of 30 μm. Similar to the 0.76 μm band, 240 pixels of spatial dimension are binned to 20 pixels for better SNR. Because the dark noise of HgCdTe detectors increases with rising temperature, a Stirling cryocooler is used to maintain the HgCdTe detectors at their operating temperature (150 K). The performance requirements of HRHS-GS are given in Table 1.

3. Spectral resolution and spectral sampling

Spectral sampling is the ratio of spectral resolution to sampling interval; it represents the number of sampling points on full-width at half-maximum (FWHM) of the ILS function. HRHS-GS has high spectral resolution and multi-spectrum channels; continuous spectrum dispersed by the diffraction grating is recorded accurately in discrete form using FPA. If the spectral resolution is equal to or smaller than the pixel interval, the spectral feature on a smaller scale will be ignored by interpolation, resulting in under-sampling. Under the same spectral resolution, higher spectral sampling results in smoother and finer absorption lines. According to the Nyquist Theorem, spectral sampling must be more than 2 in order to obtain complete spectral information, that is, the image of the slit on the FPA needs at least two pixels in the dispersion direction to sample.

Taking the 0.76 μm O_2A-band as an example, the design results of the spectrometer are given below. The spectral range of the 0.76 μm band is 0.758–0.778 μm; the spectral sampling resolution (spectral bandwidth of a single pixel) is 0.0167 nm. Figure 2 shows the optical system structure diagram of the 0.76 μm band, including four fused silica lens and one diffraction grating; the angle between the incident optical axis and the emergent optical axis is 23°; the angle between the incident optical axis and the grating

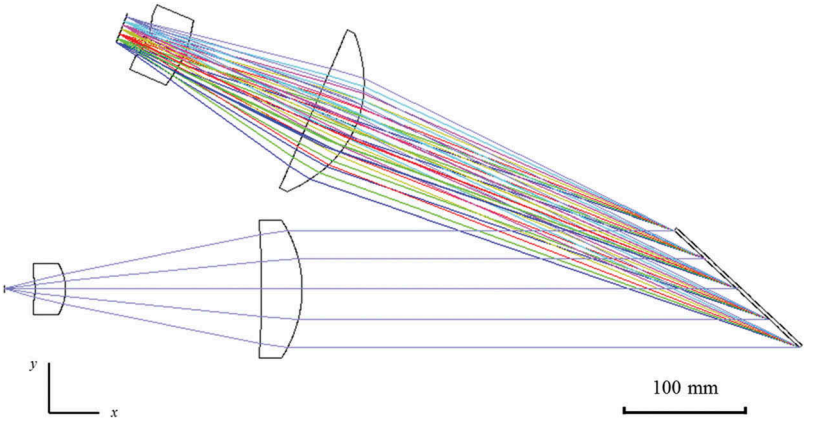

Figure 2. Optical system structure diagram of the 0.76 μm band.

is 46.2°; and the grating groove density is 2157 g mm^{-1} (Zheng et al. 2015; Mei et al. 2016).

Figure 3 illustrates the spot diagram, the modulation transfer function (MTF), the spectral enclosed energy, and the spectral sampling of the 0.76 μm band. Figure 3(a) shows the long, narrow spots with an aspect ratio consistent with the detector pixel sampling in both spatial and spectral directions; it represents the feature of the spectrometer with high spectral resolution and low spatial resolution. We can see in Figure 3(b) that the MTF on the spectral dimension of the whole field of view is larger than 0.9, and it can effectively reduce the bandwidth broadening effect due to light scattering. The pixel size on the spatial dimension is 360 μm, the corresponding Nyquist frequency is 1.39 lp mm^{-1}(line pairs per millimetre), and the MTF is greater than 0.945. Figure 3(c) illustrates that the disc of confusion on the spectral dimension is extremely small; 50% of the energy in the dispersion direction is contained within a distance of less than 0.43 μm from the image centroid, and for 99% of the energy, the energy dispersion circle radius is less than 4.6 μm. The results demonstrate that each spectral channel has high spectral purity. Figure 3(d) shows the spectral sampling of the 0.76 μm band for different wavelengths; the spectral sampling is 2.0–2.8 and the spectral resolution is 0.033–0.047 nm.

4. Laboratory calibration

4.1. *Spectral calibration*

The laboratory spectral calibration of HRHS-GS was used to determine the ILS function, the centre wavelength, and the spectral resolution. The ILS profiles were derived from the tunable diode-laser testing (Day et al. 2011; Sugavanam et al. 2016). Figure 4 shows the laser-based spectral calibration system. The 0.76 μm, 1.61 μm, and 2.06 μm bands adopted respective lasers as the light source; each laser was fibre coupled to an integrating sphere and a wavemeter for wavelength monitoring. The monochromatic collimated light uniformly illuminated the entrance telescope of HRHS-GS. The three bands scanned the respective spectral range with an interval of 0.005 nm, 0.01 nm, and

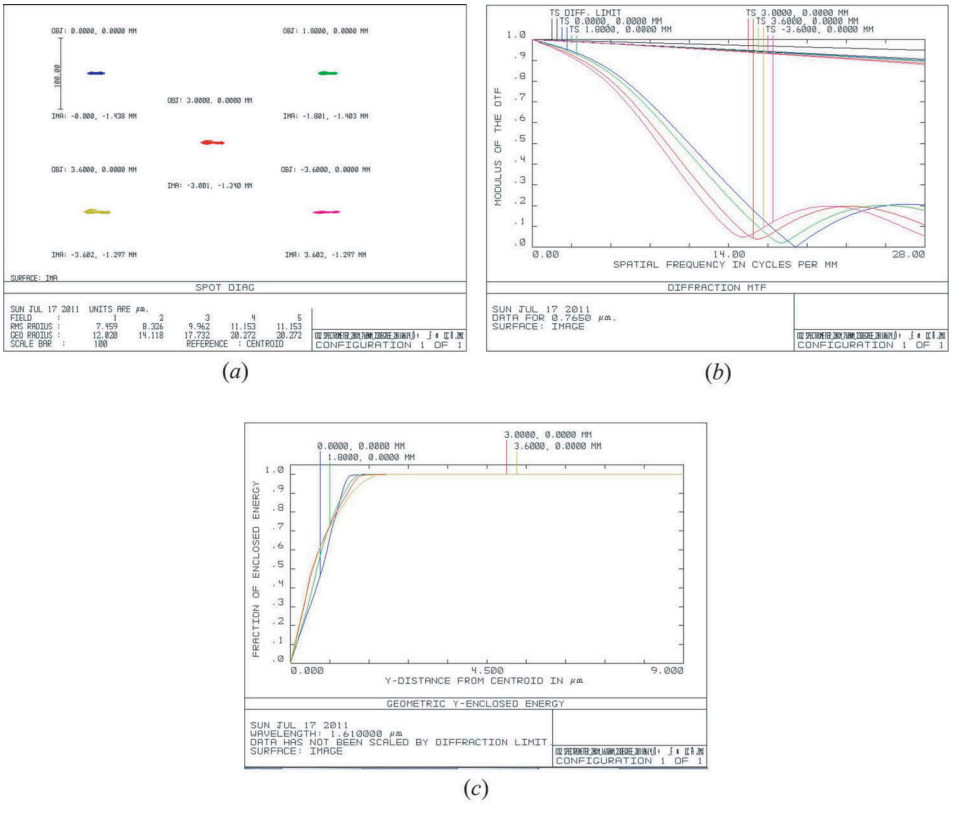

Figure 3. (a) Spot diagram of the 0.76 μm band. (b) MTF of the 0.76 μm band. (c) Spectral enclosed energy of the 0.76 μm band.

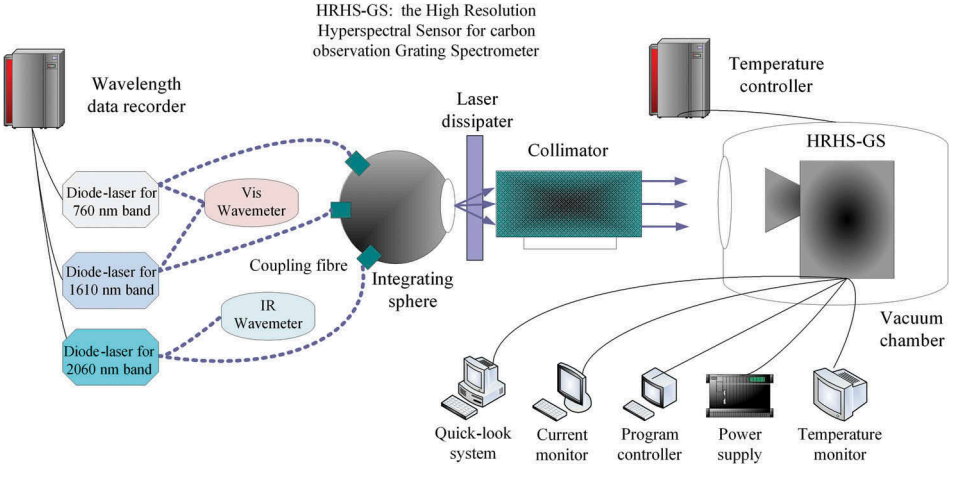

Figure 4. The laser-based spectral calibration system scheme.

0.02 nm. After power correction and normalization, the ILS of each spectral channel was obtained. The results of the laboratory laser-based calibration are shown in Figure 5–7 (Sakuma et al. 2010; Wan et al. 2015; He et al. 2016).

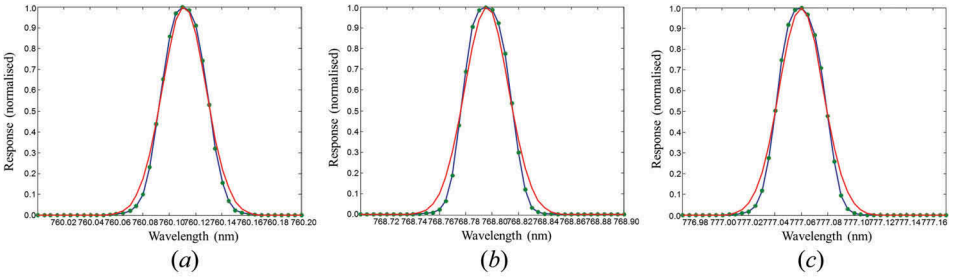

Figure 5. Spectral response function (ILS) of several different channels on three spatial positions for the 0.76 m band (FOV represents spatial pixel; Channel represents spectral pixel). (a) FOV = 3; Channel = 153; FWHM = 0.0401 nm; Centre wavelength = 760.113 nm; (b) FOV = 10; Channel = 642; FWHM = 0.0398 nm; Centre wavelength = 768.798 nm; (c) FOV = 17; Channel = 1181; FWHM = 0.0393 nm; Centre wavelength = 777.064 nm.

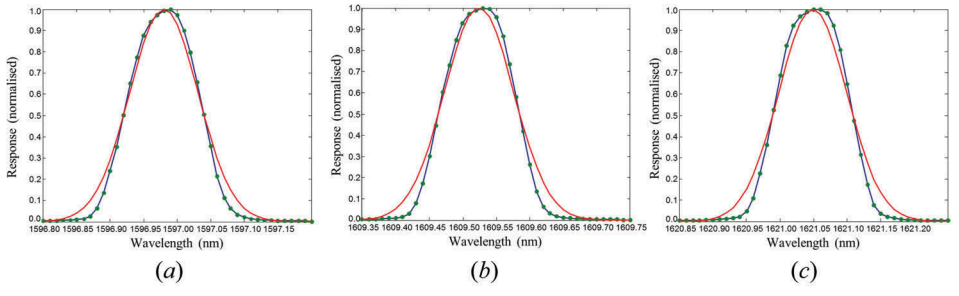

Figure 6. Spectral response function (ILS) of several different channels on three spatial positions for the 1.61 m band (FOV represents spatial pixel; Channel represents spectral pixel). (a) FOV = 3; Channel = 58; FWHM = 0.1330 nm; Center wavelength = 1596.983 nm; (b) FOV = 10; Channel = 258; FWHM = 0.1279 nm; Centre wavelength = 1609.532 nm; (c) FOV = 17; Channel = 468; FWHM = 0.1307 nm; Centre wavelength = 1621.053 nm.

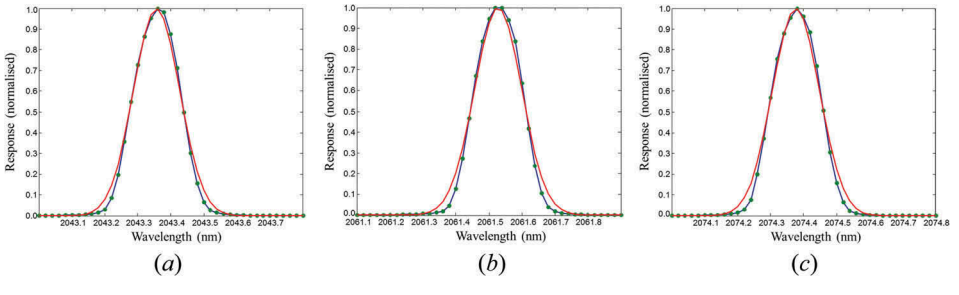

Figure 7. Spectral response function (ILS) of several different channels on three spatial positions for the 2.06 m band (FOV represents spatial pixel; Channel represents spectral pixel). (a) FOV = 3; Channel = 23; FWHM = 0.1749 nm; Center wavelength = 2043.368 nm; (b) FOV = 10; Channel = 259; FWHM = 0.1721 nm; Centre wavelength = 2061.527 nm; (c) FOV = 17; Channel = 431; FWHM = 0.1723 nm; Centre wavelength = 2074.385 nm.

According to the above-mentioned results, for the 0.76 μm band, the FWHM of the ILS is 0.04 nm±2%; for the 1.61 μm band, it is 0.13 nm±3%; and for the 2.06 μm band, it is 0.17 nm±3%. The results of spectral calibration agree well with the design values, satisfying the spectral detection requirements for high spectral resolution (Frankenberg et al. 2015; Zhang et al. 2015a).

4.2. *SNR testing*

SNR testing was performed in a thermal-vacuum chamber; the integrating sphere was placed outside of the chamber and the instrument entrance slit was fully illuminated (O'Dell et al. 2011). Two tungsten bulbs (1000 W) with a variable aperture slot illuminated the sphere; the spectral range of the sphere was 500–2500 nm, the radiation distribution temperature was 3000–3500 K, the uniformity of radiance illumination on the sphere port was better than 98%, and the consistency between radiance in all directions of the whole field of view was better than 99% (Li 2015; Liu et al. 2015). The illumination of the integrating sphere was adjusted to simulate the typical radiance on orbit (albedo 0.05). According to Equations (1) and (2), the SNR $X_{(i,j)}$(channel = i, FOV = j) can be calculated as follows:

$$X_{(i,j)} = \frac{\bar{S}}{\sqrt{\frac{1}{M-1}\sum_{k=1}^{M}\left(S_{(i,j),k} - \bar{S}\right)^2}}, \tag{1}$$

$$\bar{S} = \frac{1}{M}\sum_{k=1}^{M} S_{(i,j),k}, \tag{2}$$

where $S_{(i,j),k}$is the DN value for channel = i, FOV = j, frame = k; M is the number of frames ($M \geq 100$); and $\bar{S}$ is the average DN value.

Figure 8 shows the SNRs of the three bands for different spectral channels under typical radiance. We can see that the average SNRs of the three bands are 373.9, 221.6, and 150.7. This met the mission requirement for the 0.76 μm O_2-A band, but missed the requirements for the 1.61 μm and 2.06 μm bands.

4.3. *Multiplex merging of spectral pixels*

The SNR is directly proportional to the root mean square (RMS) of the signal intensity; the conventional approach of improving the SNR is pixel merging. Currently, sets of 16 pixels in the spatial dimension were binned to one 'big pixel', the corresponding ground resolution was 1 km × 2 km; the pixels in the spatial dimension cannot be merged again. In addition, merging of spectral pixels would reduce the spectral sampling, causing under-sampling. The feature of the absorption lines cannot be accurately described.

To improve the SNR without reducing the spectral sampling, the model 'Multiplex Merging of Spectral Pixels' was established. Specific data conversion method is shown in Figure 9. The horizontal axis is the spectral dimension, and the vertical axis is the

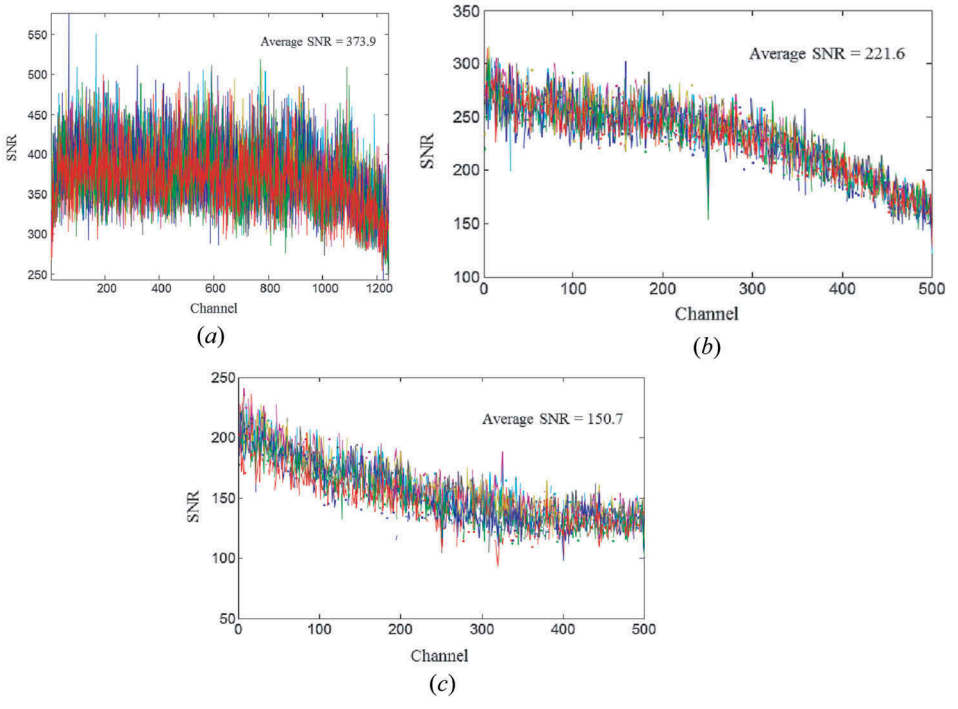

Figure 8. (a) Measured SNR for different channels in the 0.76 m band of HRHS-GS under typical radiance. (b) Measured SNR for different channels in the 1.61 m band of HRHS-GS under typical radiance. (c) Measured SNR for different channels in the 2.06 m band of HRHS-GS under typical radiance.

spatial dimension. For the spatial dimension, common pixel binning was conducted, which is not discussed here. For the spectral dimension, every two columns of data were implemented to multiplex merging. The data of the first column and the one of the second column in the spectral dimension were added to serve as the new first column in the spectral dimension; the data of the second column and the one of the third column in the spectral dimension were added to serve as the new second column in the spectral dimension, and so on ($i_1+i_2 = j_1$; $i_2+i_3 = j_2 \ldots i_{M-1}+i_M = j_{M-1}$). The signal intensity of each pixel would be doubled and the spectral sampling would almost remain unchanged (Rehman, Kumar, and Banerjee 2016; Luo et al. 2016). For the two CO_2 bands, the number of spectral sampling points would change from 500 to 499.

This kind of data processing method would cause spectral aliasing to some extent, broadening the ILS and reducing the spectral resolution of each spectral channel. Decreasing the spectral resolution would reduce the instrument sensitivity to the content of CO_2 (Cai, Liu, and Yang 2014; Shanghavi, Lebsock, and Stephens 2015). To analyse the influence and verify the feasibility of the multiplex merging of spectral pixels, the ILS and spectral resolution were compared between before and after this data processing.

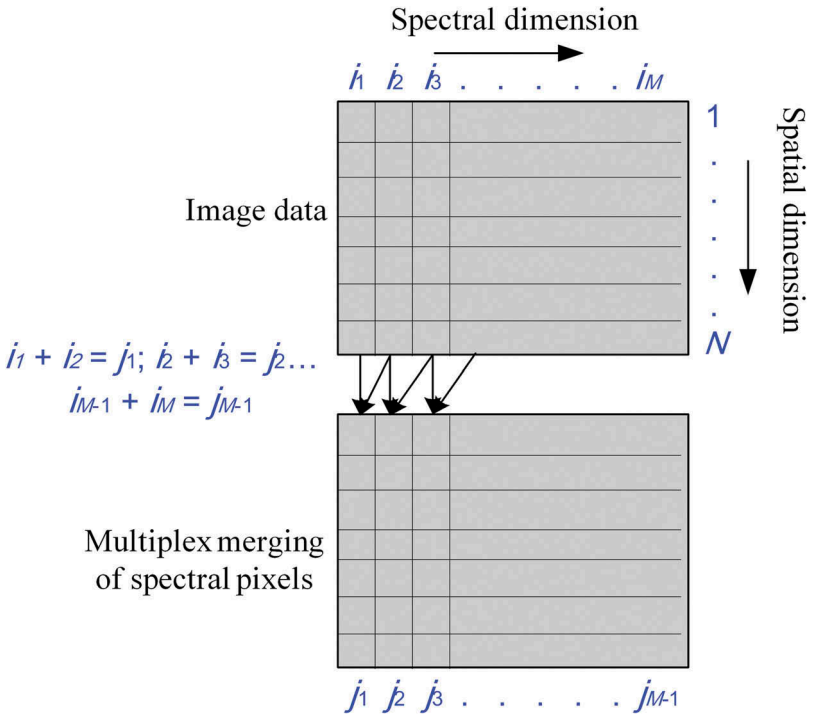

Figure 9. Sketch of the multiplex merging of spectral pixels.

5. Analysis and discussion

The ILS of each spectral channel was obtained before and after the multiplex merging of spectral pixels, and then the variation of the spectral resolution was achieved. After that, the influence on absorption lines from reducing the spectral resolution was simulated by the line-by-line radiative transfer model (LBLRTM). Finally, the results were validated by the experimental data.

5.1. *SNR improvement*

Using Equations (1) and (2), the SNRs of before and after the multiplex merging were compared for the 1.61 μm and 2.06 μm bands as shown in Figure 10. The horizontal axis is the spectral channel number, and the vertical axis is SNR. It can be seen that the variation trends of SNR are consistent before and after the multiplex merging. Thus, the average SNR of 500 spectral channels is used to represent the variation of SNR. It can be seen that the average SNR increases from 221.6 to 281.8 for the 1.61 μm band and it increases from 150.7 to 187.6 for the 2.06 μm band. In theory, SNR increases with multiplex merging following the power law, with the exponent of 0.5 of the number of multiplex pixels. The measured exponent value is 0.32–0.34 owing to diversity between the different pixels. The SNRs for the two CO_2 bands are both greatly improved and meet the mission requirement.

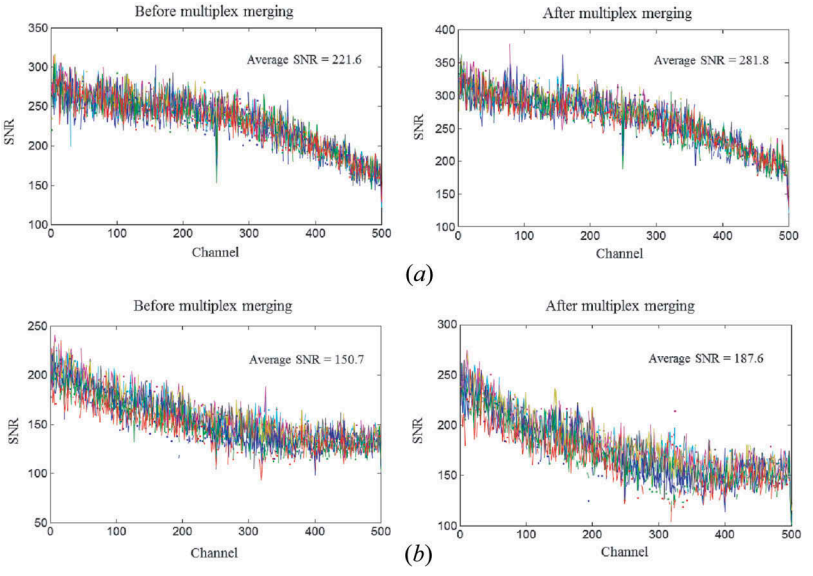

Figure 10. (a) The SNR before and after the multiplex merging for the 1.61 μm band under typical radiance. (b) The SNR before and after the multiplex merging for the 2.06 μm band under typical radiance.

5.2. *Spectral broadening*

Multiplex merging of spectral pixels would result in spectral broadening of each spectral channel. Here, the quantitative analysis was made for spectral broadening. The spectral data from laboratory calibration was processed as shown in Figure 9. For the three bands, a new ILS of each spectral channel was gained. One of them was considered to compare with the previous ILS as shown in Figure 11–13.

5.3. *Centre wavelength shift*

Besides improving SNR and spectral broadening, the method 'Multiplex Merging of Spectral Pixels' could result in centre wavelength shift. By comparing the centre wavelength of each spectral channel before and after the multiplex merging, the average values of centre wavelength shift for the three bands are given in Table 2, with 0.0104 nm, 0.0315 nm, and 0.0402 nm, respectively.

The reason that causes this shift is that the two adjacent columns of data are binned to one new column of data. The centre wavelength of the new spectral channel should infinitely approach the average value between the centre wavelengths of the two previous spectral channels. The spectral sampling rates of the three bands are 0.02 nm, 0.06 nm, and 0.08 nm, respectively. Therefore, the theoretical values of the centre wavelength shift for the three bands are 0.01 nm, 0.03 nm, and 0.04 nm, and overall shift. The experimental results are consistent with the theoretical analysis. Because of overall shift, there is no impact on gas absorption lines.

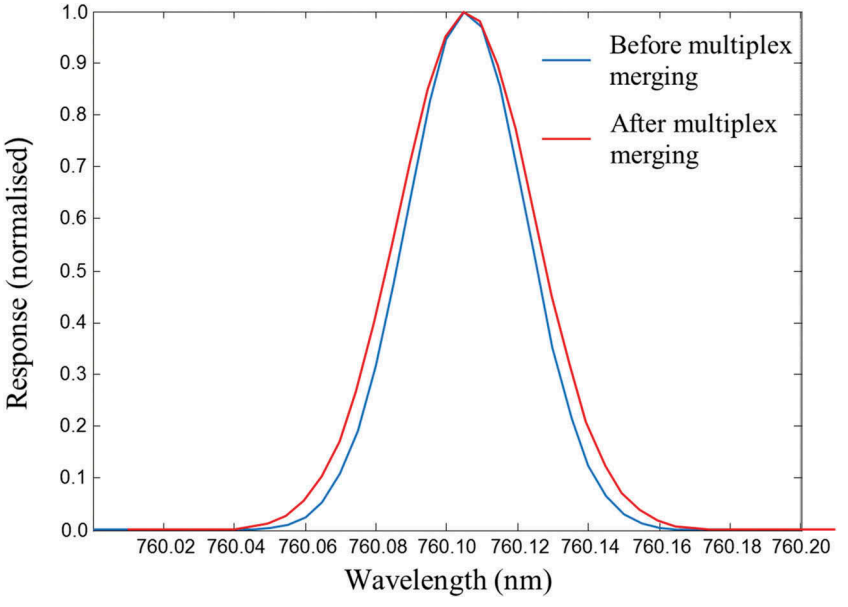

Figure 11. The ILS of the 0.76 μm band before and after the multiplex merging of spectral pixels. Blue line represents the ILS before the multiplex merging (FOV = 10; Channel = 157; FWHM = 0.0408 nm); red line represents the ILS after the multiplex merging (FOV = 10; Channel = 157; FWHM = 0.0429 nm).

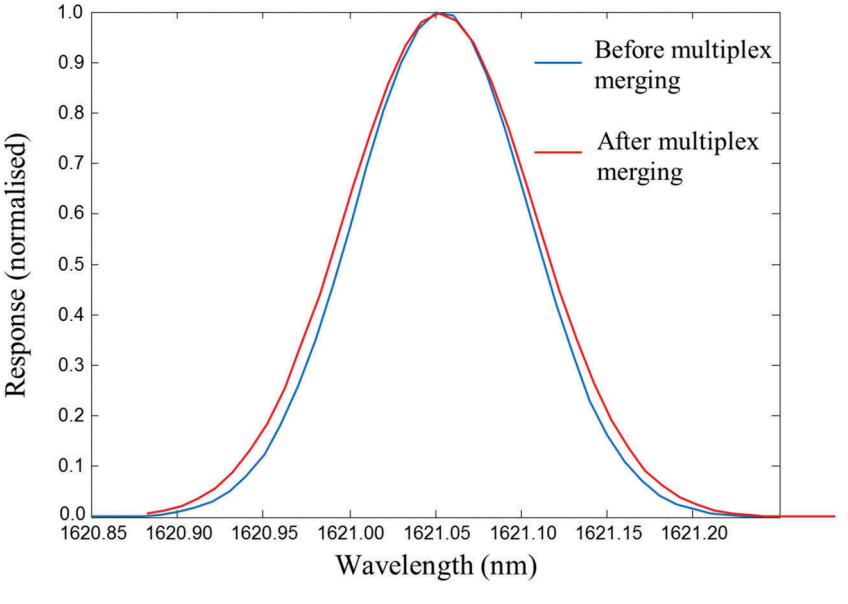

Figure 12. The ILS of the 1.61 μm band before and after the multiplex merging of spectral pixels. Blue line represents the ILS before the multiplex merging (FOV = 17; Channel = 449; FWHM = 0.1307 nm); red line represents the ILS after the multiplex merging (FOV = 17; Channel = 449; FWHM = 0.1407 nm).

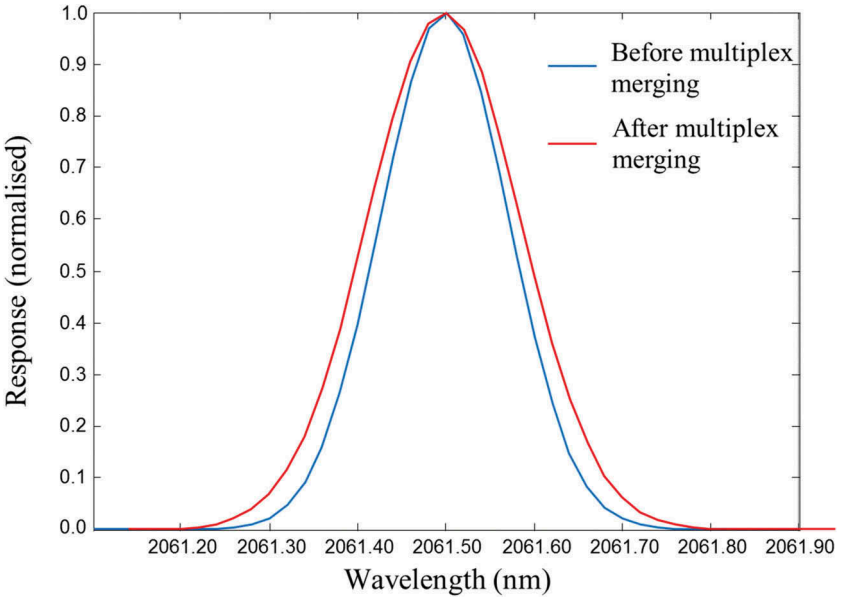

Figure 13. The ILS of the 2.06 μm band before and after the multiplex merging of spectral pixels. Blue line represents the ILS before the multiplex merging (FOV = 17; Channel = 222; FWHM = 0.1705 nm); red line represents the ILS after the multiplex merging (FOV = 17; Channel = 222; FWHM = 0.1943 nm).

Table 2. Centre wavelength shift and spectral resolution of the three bands before and after multiplex merging.

Spectral band	Spectral resolution before multiplex merging	Spectral resolution after multiplex merging	Centre wavelength Shift
0.76 μm	0.04 nm	0.0425 nm	0.0104 nm
1.61 μm	0.13 nm	0.141 nm	0.0315 nm
2.06 μm	0.169 nm	0.193 nm	0.0402 nm

5.4. *Influence on absorption lines by theoretical simulation*

'Multiplex Merging of Spectral Pixels' would result in spectral broadening. The transmittance spectra before and after merging were calculated by LBLRTM using the HITRAN 2012 database (Rothman et al. 2013), and compared as shown in Figure 14. The influence on the absorption lines from spectral broadening was analysed quantitatively (Thompson et al. 2012; Zadvornykh and Gribanov 2015).

As shown, for the 0.76 μm O_2 A-band, the transmittance spectra before and after merging are almost the same. This is because the band is used to measure atmospheric oxygen absorption; the oxygen absorption capacity for this band is extremely strong. Even if the spectral resolution reduces, the instrument can still detect the oxygen absorption lines finely. For the 1.61 μm weak CO_2 band, the peak value of the CO_2 absorption lines decays 4.2% due to spectral broadening. The atmospheric CO_2 absorbability for this band is weak; the absorption lines are sensitive to the reduction of

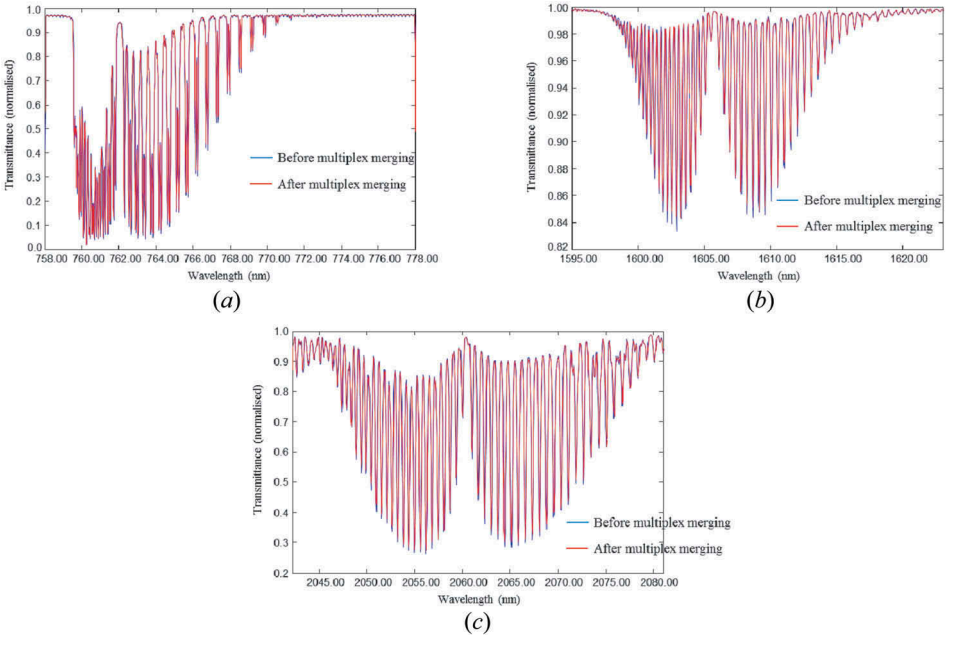

Figure 14. (a) Transmission spectra of the 0.76 μm band before and after multiplex merging by theoretical simulation. (b) Transmission spectra of the 1.61 μm band before and after multiplex merging by theoretical simulation. (c) Transmission spectra of the 2.06 μm band before and after multiplex merging by theoretical simulation.

spectral resolution. For the 2.06 μm strong CO_2 band, spectral broadening causes the peak value of the CO_2 absorption lines to decay 2.5%. Absorption of CO_2 in this band is relatively strong; despite multiplex merging of spectral pixels, spectral transmittance still achieves less than 0.3.

5.5. *Experimental verification*

To verify the theoretical results, the gas absorption cell with 33 m optical path length and 8.5 l volume was adopted. The gas absorption cell was filled with 100% O_2 and 50% CO_2 successively to measure the transmittance spectra of the three bands. Then the process of multiplex merging of spectral pixels was implemented. Figure 15 illustrates the measured transmittance spectra before and after multiplex merging, verifying the theoretical results above.

Compared with the theoretical results, it was found that the gas transmittance from the experiment is far larger than that from the theoretical simulation for the 0.76 μm band. This is because the O_2 content of the atmosphere is about 21%;the optical path length under real atmospheric conditions is 10 km (supposing the air above 10 km is very thin). Even if 100% O_2 is filled, the concentration-path length product in the gas absorption cell is still far smaller than that in the real atmosphere. For the two CO_2 bands, due to the low level of CO_2 in the atmosphere (approximately 380 ppm), the concentration of 11.5% CO_2 in the gas absorption cell is enough to simulate the real

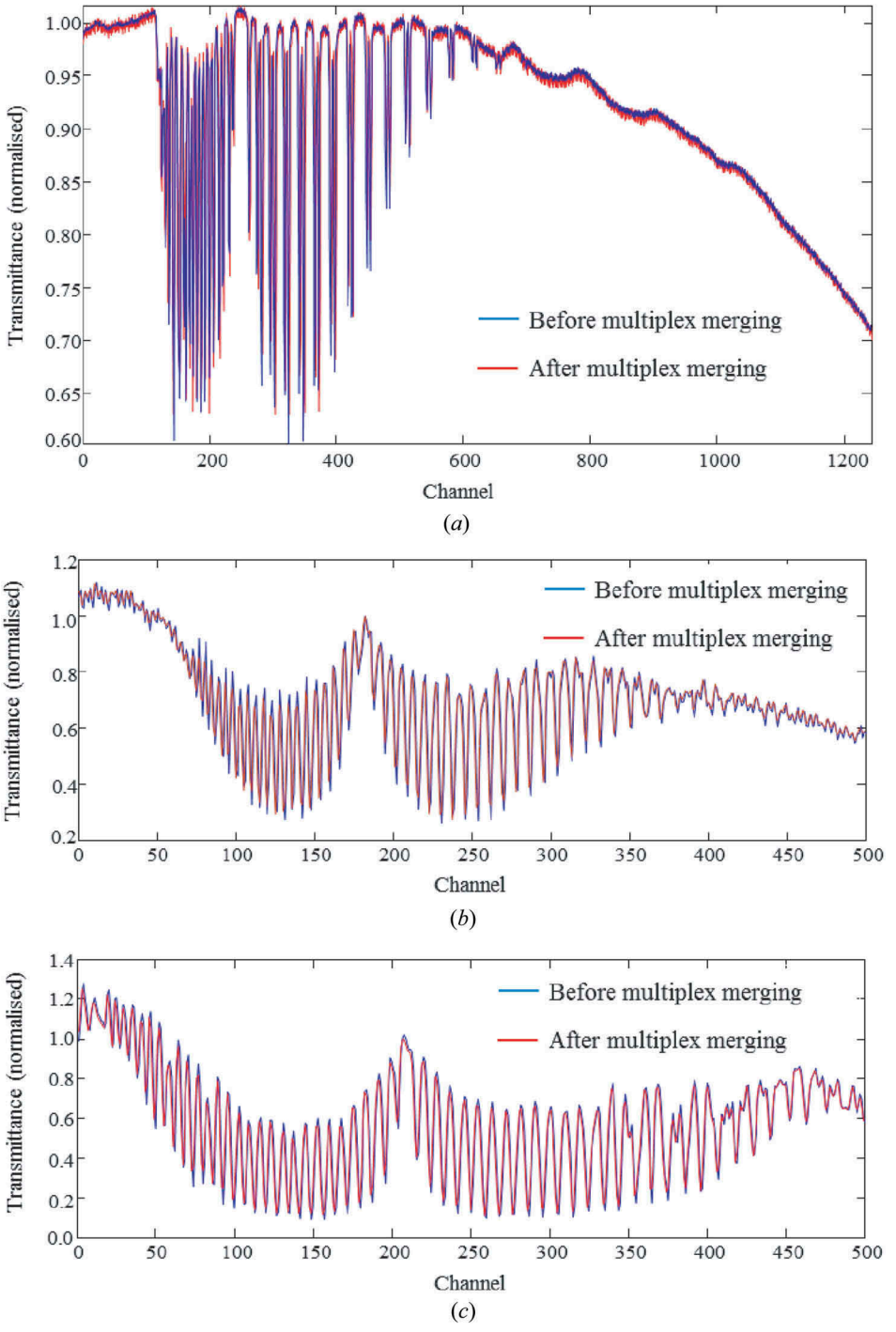

Figure 15. (a) The measured transmittance spectra before and after multiplex merging for the 0.76 μm band. (b) The measured transmittance spectra before and after multiplex merging for the 1.61 μm band. (c) The measured transmittance spectra before and after multiplex merging for the 2.06 μm band.

atmosphere condition. To describe the characteristics of CO_2 absorption lines more clearly and precisely, the concentration of CO_2 in the gas absorption cell is increased, and the dynamic range of the measured transmittance spectra is larger. Although the dynamic ranges of the transmittance spectra in the gas absorption cell and in the real atmosphere are inconsistent, their relative variations have a good consistency. For the 0.76 μm band, there is little difference between the transmittance spectra before and after multiplex merging. For the 1.61 μm and 2.06 μm bands, the maximum attenuations of the transmittance spectra after merging are, respectively, 5.1% and 2.8%.

Overall, 'Multiplex Merging of Spectral Pixels' could effectively improve SNR, but led to spectral broadening and then reduced the sensitivity of the instrument to gas contents at the same time. Through theoretical simulation and experimental verification, it was found that the spectral resolution after broadening still met the mission requirement. For the 0.76 μm band, the transmittance spectra before and after merging were almost the same. For the 1.61 μm and 2.06 μm bands, 'Multiplex Merging of Spectral Pixels' would lead to about 5% maximum attenuation of transmittance spectra.

6. Conclusion

This article first reviewed the main characteristics of HRHS-GS; the design results of the spectrometer are given. The impact of spectral sampling on instrument performance was discussed. The SNR, ILS, and spectral resolution of each channel in the three bands were obtained in the laboratory calibration. For the two CO_2 bands that failed to meet the SNR requirement, the model 'Multiplex Merging of Spectral Pixels' was established to improve the SNR. The transmittance spectra before and after merging were compared through theoretical simulation and experimental verification. The results showed that 'Multiplex Merging of Spectral Pixels' could effectively improve SNR; the spectral resolution after merging still satisfied the mission requirements and the transmittance spectra still demonstrated the feature of the gas absorption lines well.

Acknowledgements

The authors would like to thank every member of Carbon Observing Satellite science team for their contribution and kind support. This work was supported by the National High Technology Research and Development Program of China (No. 2011AA12A102).

Disclosure statement

No potential conflict of interest was reported by the authors.

Funding

This work was supported by the Ministry of Science and Technology under the National High Technology Research and Development Program of China (863 Program) (number 2011AA12A102).

References

Bai, Y., Z. Liao, S. Liao, Q. Ren, and W. Chen. 2016. "Infrared Dual Band Athermal Optical System with Common Aperture." *Optics and Precision Engneering* 24 (2): 268–277. doi:10.3788/OPE.20162402.0268.

Basilio, R. R., H. R. Pollock, and S. L. Hunyadi-Lay. 2014. "OCO-2 (Orbiting Carbon Observatory-2) Mission Operations Planning and Initial Operations Experiences." *Proceedings of SPIE* 9241: 924105.

Bi, Y. M., Q. Wang, Z. D. Yang, S. Y. Gu, R. H. Wu, and C. B. Liu. 2015. "Advances on Space-Based Hyper Spectral Remote Sensing for Atmospheric CO2 in near Infrared Band." *Chinese Optics* 8 (5): 725–735. doi:10.3788/co.20150805.0725.

Cai, Z. N., Y. Liu, and D. X. Yang. 2014. "Analysis of XCO2 Retrieval Sensitivity Using Simulated Chinese Carbon Satellite (Tansat) Measurements." *Science China-Earth Sciences* 57 (8): 1919–1928. doi:10.1007/s11430-013-4707-1.

Crisp, D. 2015. "Measuring Atmospheric Carbon Dioxide from Space with the Orbiting Carbon Observatory-2 (OCO-2)." *Proceedings of SPIE* 9607: 960702.

Crisp, D., C. E. Miller, and P. L. De Cola. 2008. ""NASA Orbiting Carbon Observatory: Measuring the Column Averaged Carbon Dioxide Mole Fraction from Space,"." *Journal of Applied Remote Sensing* 2 (1): 1–14. doi:10.1117/1.2898457.

Cu-Nguyen, P., A. Grewe, P. Feber, A. Seifert, S. Sinzinger, and H. Zappe. 2016. "An Imaging Spectrometer Employing Tunable Hyperchromatic Microlenses." *Light: Science and Application* 5. doi:10.1038/lsa.2016.58.

Day, J. O., C. W. O'Dell, R. Pollock, and C. J. Bruegge. 2011. "Preflight Spectral Calibration of the Orbiting Carbon Observatory." *IEEE Transactions on Geoscience and Remote Sensing* 49 (7): 2793–2801. doi:10.1109/TGRS.2011.2107745.

Eldering, A., S. Boland, B. Solish, D. Crisp, P. Kahn, and M. Gunson. 2012. "High Precision Atmospheric CO2 Measurements from Space: The Design and Implementation of OCO-2." *In Proceedings of the IEEE Aerospace Conference* 186 (6): 1–10.

Frankenberg, C., R. Pollock, R. Lee, R. Rosenberg, and J. F. Blavier. 2015. "The Orbiting Carbon Observatory (OCO-2): Spectrometer Performance Evaluation Using Pre-Launch Direct Sun Measurements." *Atmospheric Measure Techniques* 8: 301–313. doi:10.5194/amt-8-301-2015.

He, L., B. Chen, H. Zhang, S. Liu, and X. Wang. 2016. "Radiation Calibration of EUV Space Cameras." *Optics and Precision Engneering* 24 (5): 1867–1873.

Kuze, A., T. Urbe, H. Suto, and T. Hamazaki. 2006. "The Instrumentation and the BBM Test Results of Thermal and near Infrared Sensor for Carbon Observation (TANSO) on GOSAT." *Proceedings of SPIE* 6297: 62970K.

Laurenza, L. M., S. D. Bianco, M. Gai, F. Barbara, G. Schiavon, and U. Cortesi. 2014. "Comparison of Column-Averaged Volume Mixing Ratios of Carbon Dioxide Retrieved from IASI/METOP-A Using KLIMA Algorithm and TANSOFTS/GOSAT Level 2 Products." *IEEE Journal of Selected Topics in Applied Earth Observations and Remote Sensing* 7 (2): 389–398. doi:10.1109/JSTARS.2013.2276125.

Li, Z. 2015. ""High Accuracy Spectroradiometric Standard Light Source Based on Detector Standard." *Chinese Optical* 8 (6): 908–918.

Liu, Y., M. Duan, Z. Cai, D. Yang, D. Lu, Z. Yin, Y. Zheng, C. Yan, and Z. Yang. 2012. "Chinese Carbon Dioxide Satellite (Tansat) Status and Plans." *In Proceedings of American Geophysical Union 2012 Fall Meeting, American Geophysical Union*.

Liu, Z., Z. Wan, X. Li, B. Li, and Y. Shao. 2015. "Influence Factors on SNR of TDICCD Space Camera." *Optics and Precision Engneering* 23 (7): 1829–1837. doi:10.3788/OPE.20152307.1829.

Luo, W., Y. Zhang, A. Feizi, Z. Gorocs, and A. Ozcan. 2016. "Pixel Super-Resolution Using Wavelength Scanning." *Light: Science and Application* 5. doi:10.1038/lsa.2016.60.

Mei, G., Y. Zhai, J. Miao, Q. Pu, and D. Yu. 2016. "Focal Plane Alignment and Testing for an Off-Axis Multispectral Space Borne Camera." *Chinese Optics* 9 (4): 491–500. doi:10.3788/co.20160904.0491.

O'Dell, C. W., J. O. Day, R. Pollock, C. J. Bruegge, and D. M. O'Brien. 2011. "Preflight Radiometric Calibration of the Orbiting Carbon Observatory." *IEEE Transactions on Geoscience and Remote Sensing* 49 (6): 2438–2447. doi:10.1109/TGRS.2010.2090887.

Rehman, S. U., A. Kumar, and A. Banerjee. 2016. "SNR Improvement for Hyperspectral Application Using Frame and Pixel Binning." *Proceedings of SPIE* 9881: 98810Y.

Rothman, L. S., I. E. Gordon, Y. Babikov, A. Barbe, D. C. Benner, P. F. Bernath, M. Birk, et al. 2013. "The HITRAN 2012 Molecular Spectroscopic Database". *Journal of Quantitative Spectroscopy and Radiative Transfer* 130: 4–50. doi:10.1016/j.jqsrt.2013.07.002.

Sakuma, F., C. J. Bruegge, D. Rider, D. Brown, and S. Geier. 2010. "OCO/GOSAT Preflight Cross-Calibration Experiment." *IEEE Transactions on Geoscience and Remote Sensing* 48 (1): 585–599. doi:10.1109/TGRS.2009.2026050.

Shanghavi, S., M. Lebsock, and G. Stephens. 2015. "Sensitivity Analysis of Polarimetric O_2 A-Band Spectra for Potential Cloud Retrievals Using OCO-2/GOSAT Measurements." *Atmospheric Measure Techniques* 8: 3601–3616. doi:10.5194/amt-8-3601-2015.

Sugavanam, S., S. Fabbri, S. T. Le, I. Lobach, and S. Kablukov. 2016. "Real-Time High-Resolution Heterodyne-Based Measurements of Spectral Dynamics in Fibre Lasers." *Light: Science and Application* 6: 231152.

Thompson, D. R., D. C. Benner, L. R. Brown, D. Crisp, and V. M. Devi. 2012. "Atmospheric Validation of High Accuracy CO2 Absorption Coefficients for the OCO-2 Mission." *Journal of Quantitative Spectroscopy and Radiative Transfer* 113: 2265–2276. doi:10.1016/j.jqsrt.2012.05.021.

Wan, Z., B. Li, Z. Liu, H. Liu, and J. Ren. 2015. "Spectral and Radiometric Calibrations for Mapping Satellite-1 Camera." *Optics and Precision Engneering* 23 (7): 1867–1873. doi:10.3788/OPE.20152307.1867.

Zadvornykh, I. V., and K. G. Gribanov. 2015. "Testing Forward Model against OCO-2 and TANSO-FTS/GOSAT Observed Spectra in near Infrared Range." *Proceedings of SPIE* 9680: 968002.

Zhang, H., Y. Zheng, W. Wang, C. Lin, D. Liu, and S. Li. 2015a. "Spectral Detection with High Spectral Resolution and High Signal-To-Noise Ratio Based on Remote Sensing Monitoring." *Optics and Precision Engneering* 23 (10): 229–238. doi:10.3788/OPE.2152313.0229.

Zhang, J., J. Shao, and C. Yan. 2015. "Cloud and Aerosol Polarimetric Imager." *Proceedings of SPIE* 9142: 91420X.

Zhang, J., C. Xue, Z. Gao, and C. Yan. 2015b. "Optical Remote Sensor for Cloud and Aerosol from Space: Past, Present and Future." *Chinese Optics* 8 (5): 679–698. doi:10.3788/co.20150805.0679.

Zheng, C., C. Lin, L. Wang, Z. Ji, and Y. Zheng. 2015. "Fine Optical Focusing of 1610 Nm Channel of CO2 Spectrometer." *Chinese Optics* 8 (6): 942–950. doi:10.3788/co.20150806.0942.